nature geoscience

ARTICLES

https://doi.org/10.1038/s41561-020-00680-2

Abrupt changes in the global carbon cycle during the last glacial period

Thomas K. Bauska[1,4] ✉, Shaun A. Marcott[2,4] ✉ and Edward J. Brook[3]

During the last glacial period, atmospheric carbon dioxide (CO_2) closely followed Antarctic temperature on millennial timescales. This strong correlation between Antarctic climate and atmospheric CO_2 has led to suggestions that reorganizations of Southern Ocean circulation and/or biogeochemistry were the dominant cause of these variations. However, recent work also revealed centennial-scale changes in CO_2 that appear unrelated to Antarctic climate and may represent additional modes of carbon cycle variability. Here we present a high-resolution CO_2 record from the last glacial period from an ice core drilled in West Antarctica. This reconstruction precisely defines the timing of millennial and centennial CO_2 variations with respect to Antarctic temperature and abrupt changes in Northern Hemisphere climate during Heinrich stadials and Dansgaard–Oeschger events. On the millennial scale, CO_2 tracks Antarctic climate variability, but peak CO_2 levels lag peak Antarctic temperature by more than 500 years. Centennial-scale CO_2 increases of up to 10 ppm occurred within some Heinrich stadials, and increases of ~5 ppm occurred at the abrupt warming of most Dansgaard–Oeschger events. Regression analysis suggests that the CO_2 variations can be explained by a combination of one mechanism operating on the timescale of Antarctic climate variability and a second responding on the timescale of Dansgaard–Oeschger events. Consistent with our statistical analysis, carbon cycle box-model simulations illustrate a plausible scenario where Southern Hemisphere processes contribute the majority of the CO_2 variability during the last glacial period, but Northern Hemisphere processes are the crucial drivers of centennial-scale variability.

The last glacial period is punctuated by multiple abrupt shifts in climate[1]. Referred to as Dansgaard–Oeschger (DO) events, their best-known fingerprints are the decadal-scale warmings and coolings over Greenland of >10 °C (refs. [2,3]). Some of the cold periods (stadials) are closely associated with the occurrence of extensive ice-rafted debris in the North Atlantic known as Heinrich events. The impacts of these rapid changes are found in a number of palaeoclimate records around the world, including atmospheric methane (CH_4) variations, which closely mimic Greenland temperature despite being mostly sourced from the tropics[3–5]. DO events are commonly ascribed to changes in the Atlantic meridional overturning circulation and atmospheric circulation that redistribute heat between the Northern and Southern hemispheres[6–9].

In Antarctica, a series of Antarctic isotope maximum (AIM) events[10] form the counterpart of the DO events[11]. Carbon dioxide (CO_2) concentrations closely track these changes in Antarctic ice-core isotopic records[12], which reflect site temperature but are also influenced by other hydrological processes[13]. CO_2 is also closely linked to changes in dust delivery to Antarctica (typically traced with ice-core Ca concentrations) with lower atmospheric CO_2 associated with higher dust deposition and more iron delivery to the Southern Ocean[14]. CO_2 similarly tracks the Antarctic ice-core record of Na, a promising yet imperfect proxy for sea-ice extent[15,16], and may indicate lower atmospheric CO_2 during periods of greater Antarctic sea ice[17].

The ice-core gas records thus far provide two invaluable tracers of global-scale biogeochemistry with no relative chronological uncertainty: millennial-scale CH_4 variations that are largely driven by changes in tropical wetland emissions[5,18] and CO_2 variations that are often ascribed to changes in the Southern Ocean carbon budget[19–23]. Previous work has shown that CO_2 starts increasing during the longer Greenlandic stadials and continues to rise after the warming that terminates the stadial[19,20]. This has been used as evidence of a slow response of the Southern Ocean carbon cycle to millennial-scale climate variability—in particular, a phenomenon that emerges only in glacial climates[20]. From a data perspective, the current paradigm is that the majority of the CO_2 variability is driven by a Southern Ocean process with a very long response time and is thus only indirectly related to DO events. The impact of short-lived DO events on CO_2 is thus thought to be negligible[24], and any CO_2 rise after the largest DO warmings is viewed as a consequence of the sluggish response of the Southern Ocean[20]. The synchronicity of abrupt CH_4 and CO_2 changes during the last deglaciation[25] and high-resolution measurements across a single DO event[26] challenge this traditional viewpoint and motivate further investigation of whether centennial-scale changes are a common feature of the glacial period CO_2 history and their potential sources. From a dynamical modelling perspective, models do not agree as to the magnitude or even the sign of change of CO_2 during stadial-like simulations[27]. This is in part due to competing contributions from terrestrial sources, where models often disagree as to the sign of the change, and oceanic sources, where models disagree as to the dominant source region. These combinations can lead to some models producing rapid increases in CO_2 during the onset of interstadial conditions[28–30] but again disagreeing as to the source(s) of CO_2 to the atmosphere.

In this article, we present a new high-resolution record of atmospheric CO_2 from the West Antarctic Ice Sheet (WAIS) Divide (WD) ice core at unprecedented resolution through the last glacial cycle, along with new carbon cycle modelling experiments. We compare

[1]British Antarctic Survey, Cambridge, UK. [2]Department of Geoscience, University of Wisconsin-Madison, Madison, WI, USA. [3]College of Earth, Ocean, and Atmospheric Sciences, Oregon State University, Corvallis, OR, USA. [4]These authors contributed equally: Thomas K. Bauska, Shaun A. Marcott. ✉e-mail: thausk@bas.ac.uk; smarcott@wisc.edu

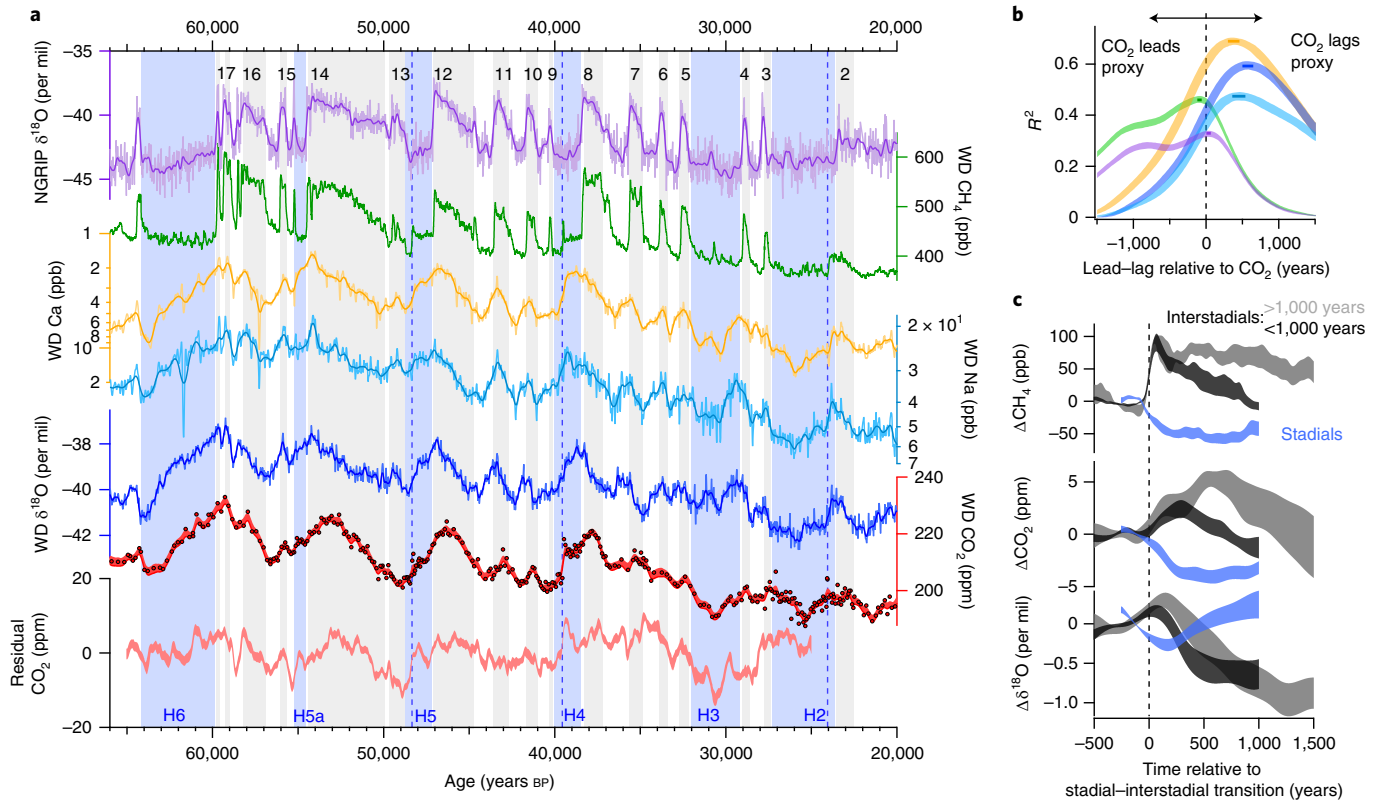

Fig. 1 | Ice-core records of polar climate, greenhouse gas variability and lead–lag correlations. a, From top to bottom: NGRIP $\delta^{18}O$ (ref. [34]), WD CH_4 (ref. [5]), log(Ca) (refs. [35,36]), log(Na) (refs. [35,36]), WD $\delta^{18}O$ (ref. [11]), WD CO_2 (this study) and residual variability in the CO_2 record not explained by a simple lagged (580 years) response to WD $\delta^{18}O$ (this study). Grey bars indicate interstadials in Greenland. Blue bars denote Heinrich stadials, with the dashed line showing the onset of the H5, H4 and H2 events as proposed in ref. [5]. **b**, The lead–lag correlation of the ice-core proxies with respect to CO_2 (colours are the same as in Fig. 1a). Shading shows the uncertainty introduced from Monte Carlo error estimates in the delta-age history (90% CI). The maximum reached in each curve indicates the apparent lead–lag with the horizontal bars indicating the range in maximum R^2 values from the delta-age histories. **c**, The evolution of WD CH_4, CO_2 and $\delta^{18}O$ after the onset of interstadial and stadial conditions. Shading shows the 1σ standard error of the stacked records divided between DO interstadials longer than 1,000 years (light grey, $n=5$), interstadials shorter than 1,000 years (dark grey, $n=10$) and all stadials (blue, $n=15$). DO9 is excluded in all stacks as the window extends into the large CO_2 jump at H4. Time series are anomalies relative to the mean of the first 500 years for interstadials and 250 years for stadials.

our CO_2 data and modelling results with other high-resolution ice-core proxies of carbon cycle-relevant processes to evaluate whether the Southern Ocean dominated glacial-period CO_2 variability. Understanding when and how these changes occur provides further insight into the processes that regulate atmospheric CO_2.

CO_2 variability during the last glacial period

In this study, we made approximately 770 CO_2 measurements on 350 sample depths from the WD ice core applying a mechanical crushing system[25,31] at Oregon State University. The measurements span 67,000–23,000 years BP with a median sampling resolution of 110 years. All samples were measured at least in duplicate, and the mean standard error of replicate measurements was 0.7 ppm. We use the previously described WD2014 gas and ice chronology[32,33]. A critical aspect of WD2014 before ~30,000 years BP is that the gas-phase chronology is synchronized to the radiometrically dated Hulu Cave oxygen isotope record using the WD CH_4 record. The chronologies for ice-phase records are then derived from the gas chronology using a model to determine the difference in age between the gas and ice phases (delta age)[11]. Crucially, delta age is relatively invariant and well constrained in the last glacial period compared with most other deep ice cores (approximately 260 ± 50 years at 60,000 years BP to a maximum of 520 ± 120 years at 20,000 years BP). We can thus precisely determine the timing of changes in CO_2 relative to the chemical and isotopic composition of the ice, whereas previous studies[20,24] could precisely determine only the timing of the gas-phase species (the phasing between CO_2 and CH_4) (Extended Data Figs. 1 and 2).

To first order, the WD CO_2 record closely tracks WD records of $\delta^{18}O$, log(Ca) and log(Na) on millennial timescales (Fig. 1a). This is consistent with previous ice-core records[19,20], but the resolution and delta-age accuracy of the WD data reveal a nuanced relationship on submillennial timescales. Most notably, the peak values in CO_2 typically lag peak values in $\delta^{18}O$, log(Ca) and log(Na), although to variable degrees. The lag appears absent near DO 17 and the rapid succession of short-lived interstadials that follow, but appears prominently at long-lived DO 14, 12 and 8 (Fig. 1a). A lead–lag correlation analysis (Extended Data Fig. 3) across the bulk of the linearly detrended record (65,000–25,000 years BP) reveals that, on average, CO_2 lags changes in WD $\delta^{18}O$, log(Ca) and log(Na) by 580 years (500–650, 90% confidence interval (CI)), 360 years (300–460, 90% CI), and 460 years (380–540, 90% CI), respectively, with only minor errors introduced from uncertainty in delta age (Fig. 1b). On the basis of the maximum R^2 value from the regression analysis, WD $\delta^{18}O$, log(Ca) and log(Na) could, respectively, explain approximately 60%, 70% and 48% of the CO_2 record, neglecting the long-term decrease into the glacial removed by detrending. All of these proxies are thought to reflect processes that govern the carbon cycle

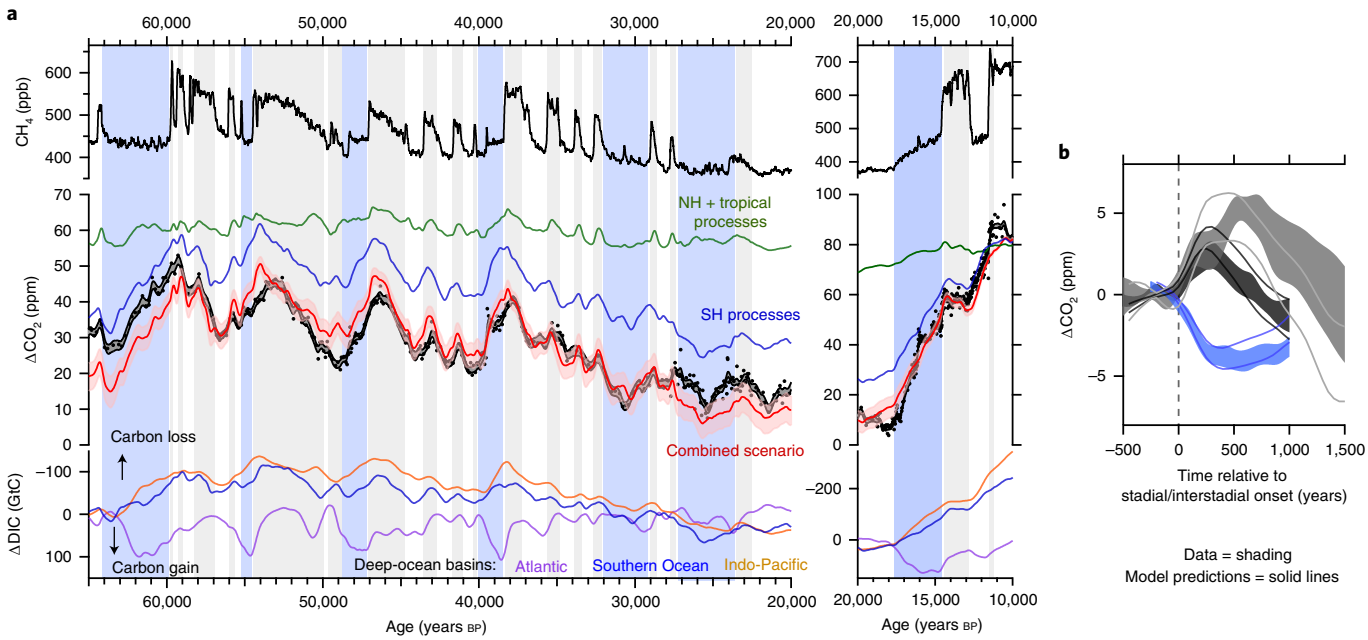

Fig. 2 | Box-model experiments illustrating a plausible scenario for last glacial period CO_2 variability. a, WD CH_4 (ref. [5]) and CO_2 data (both black) with model experiments showing an ensemble solution (red line with shading showing the 1σ standard deviation) and carbon stock anomalies of dissolved inorganic carbon (DIC) in the deep Atlantic (purple), deep Southern Ocean (blue) and deep Indo-Pacific (orange). Also shown are factorial experiments for Northern Hemisphere (NH) and tropical processes (North Atlantic sea surface temperature (SST), NADW formation and low-latitude ocean SST) (green line) and Southern Hemisphere (SH) processes (AABW formation, iron fertilization, Antarctic sea ice, and sub-Antarctic and Antarctic SST) (blue line). All model predictions are plotted as anomalies for clarity. **b**, The 1σ standard error of the stacked records of CO_2 for interstadials longer than 1,000 years (grey shading), interstadials shorter than 1,000 years (black shading) and all stadials (blue shading) as in Fig. 1c along with the same analysis for the model prediction (solid lines).

response of the deep Southern Ocean. A similar analysis passing the various proxy time series through a one-box model with variable e-folding timescales, to mimic the response time of CO_2 to a perturbation of the atmospheric budget, yields comparable characteristic timescales (Extended Data Fig. 4). Thus, these apparent lags can be considered at face value indicative of the overall response time of the deep-ocean reservoir during this time interval.

However, the three Southern Hemisphere proxies, either alone or in combination, cannot account for all the observed variability. To visualize this unaccounted-for variability, we calculated the residuals from the linear regression of the detrended WD CO_2 and $\delta^{18}O$ time series applying a 580-year lag (Fig. 1a). The resulting time series shows a mixture of variability with rapid increases in CO_2 within some of the Heinrich stadials and smaller increases at the onset of DO events. Lead–lag analysis (Fig. 1a) of North Greenland Ice Core Project (NGRIP) water isotope and WD CH_4 records against the detrended CO_2 record shows a notable maximum in the correlation with nearly zero lag (or alternatively an e-folding timescale of <100 years, Extended Data Fig. 4). Both NGRIP isotopes and WD CH_4 have a time evolution history that is more sawtooth compared with the triangular shape of the CO_2 record; therefore, a detailed interpretation of the lead–lag correlation is not straightforward[37], but the results suggest that part of the CO_2 variability could be due to a fast-acting carbon cycle process on a DO-like timescale.

To examine this in greater detail, we evaluate the mean evolution of CH_4, CO_2 and $\delta^{18}O$ after the onset of interstadial and stadial conditions (Fig. 1c). Similar to Siple Dome CO_2 measurements from ~40 to 20 thousand years ago (ka) (refs. [24,26]), we do not observe rises in CO_2 among short-lived stadials but instead small decreases that are partially influenced by the overall long-term trend to lower CO_2 towards the glacial. This decrease is present at the onset of some longer stadials (for example, HS6, HS5a, HS3 and HS2). The overall gradual rise of CO_2 during Heinrich stadials is consistent with previous records[20], but our more-detailed measurements within Heinrich stadials confirm the rapid rise in CO_2 during HS4 (refs. [23,26]) and identify a similar feature during HS5 (Fig. 3).

On the basis of our high-resolution measurements from WD, the increases in atmospheric CO_2 after the onset of interstadials are now clearly illuminated (Fig. 1c). These rises usually occur as $\delta^{18}O$, Ca and Na return to cold-phase levels in a given AIM cycle. On average, CO_2 increases by 5 ppm for each interstadial, with the largest increase of 10 ppm at DO12. This mode of variability becomes more muted after ~40 ka and can sometimes be absent, such as during DO13. We observe no significant difference in the CO_2 response if the preceding stadials contain a Heinrich event, although this observation may be influenced by the muted responses at HS3 and HS2. Similarly, there is no relationship to previous stadial length, but this may be influenced by the very long stadials 18 and 3 that are followed by only modest increases in CO_2. A statistically weak correlation is observed between CO_2 increase and length of interstadial ($r = 0.54$; $P = 0.04$) (Extended Data Fig. 5). Taken together, these observations suggest a potential driver related directly to interstadial conditions rather than the previous stadial.

Carbon cycle modelling

To further test the links between CO_2 and the potential mechanisms for the increases within interstadials, we perform carbon cycle box-model simulations to examine the interplay of Northern Hemisphere and Southern Hemisphere processes. The approach is similar to our time-series analysis in which we assume an external forcing, except we now apply a model with physical and biogeochemical constraints that realistically simulates lags and interactions in the carbon cycle[38]. The forcings can be categorized into two broad carbon cycle processes: one that operates on the timing of abrupt changes in the high-latitude Northern Hemisphere and another that operates on the timing of millennial changes in the high-latitude

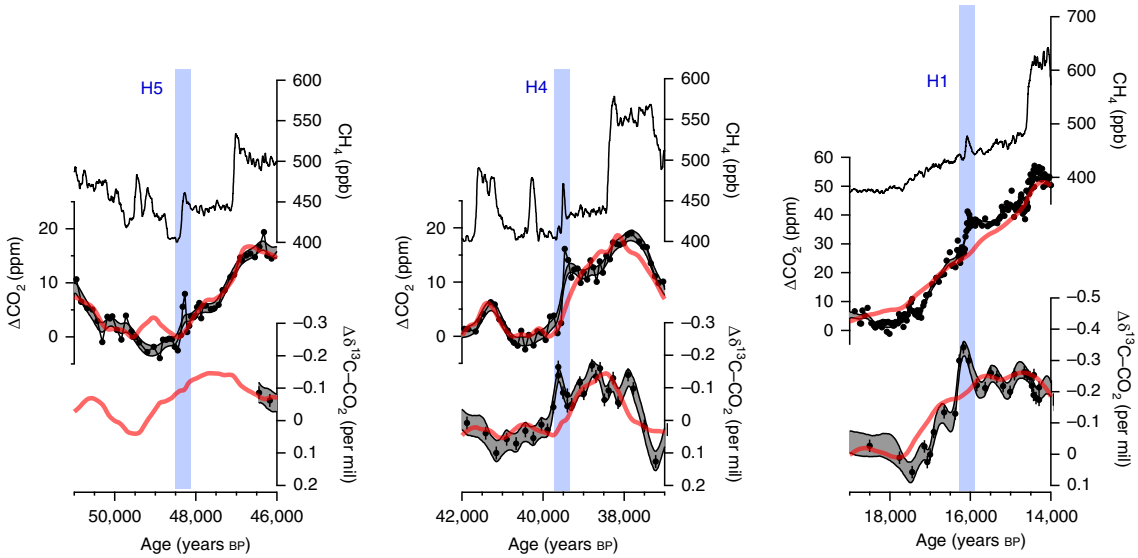

Fig. 3 | Centennial-scale greenhouse gas variability within Heinrich stadials. CO_2 (this study and ref. [25]), CH_4 (ref. [5]) and $\delta^{13}C$-CO_2 (refs. [23,38]) during Heinrich stadials 5, 4 and 1. Note the inverted *y* axis for $\delta^{13}C$-CO_2. The data are overlaid with the best-fit model solution of CO_2 and $\delta^{13}C$-CO_2 (red line) and offset to show divergence during the mid-stadial abrupt CO_2 changes. The blue bar highlights abrupt CO_2 rises that are associated with similarly abrupt rises in CH_4 and decreases in $\delta^{13}C$-CO_2, suggesting that the model is missing an injection of isotopically light carbon within a Heinrich stadial that is linked to processes that cause the abrupt rise in CH_4.

Southern Hemisphere. Our definition of forcing is restricted to the origin of the effect on the carbon cycle as we do not treat climate processes and linkages explicitly (Methods).

Southern Hemisphere processes are driven using combinations of WD Ca, Na and $\delta^{18}O$ to represent iron fertilization (modified in the model via nutrient-limiting levels of PO_4 in the Southern Ocean), Antarctic sea-ice extent and formation rate of Antarctic Bottom Water (AABW), respectively. Changes in the temperature of the sub-Antarctic and Antarctic surface ocean are driven by well-dated, latitude-binned temperature stacks during the last deglaciation[39,40] and extended into the glacial by scaling the WD $\delta^{18}O$ record[25,41] to match the overall glacial–interglacial change (Extended Data Fig. 6). Additional changes in the low-latitude, tropical ocean temperature are similarly forced by the temperature stacks during the deglaciation, but sparse data availability in the glacial requires us to extend the forcing using the total radiative forcing from CO_2, CH_4 and N_2O. North Atlantic temperatures are driven by NGRIP $\delta^{18}O$ (ref. [31]) and the overturning strength of North Atlantic Deep Water (NADW) by the Pa/Th record from Bermuda Rise[42,43] to represent Northern Hemisphere processes. Changes in glacial–interglacial land carbon storage and reef building are prescribed following previous estimates[44] and contribute primarily to the CO_2 changes in the Holocene that are outside the scope of this study.

To arrive at illustrative scenarios, we run the model with a wide range of scalings for each time series ($n = 500$, Extended Data Fig. 6). Each time series preserves the underlying structure of the proxy data and is scaled between 50% and 100% of the maximum effect allowed by the model (Extended Data Figs. 7 and 8). The temperature forcings are also varied but with scalings of ±20% of the glacial–interglacial range. This approach allows us to objectively address the relative importance of a given effect but relies on the assumption that the proxies are linearly related to the forcing. We then determine the best-fit model runs by minimization of the mean-normalized root mean square error (RMSE) between the model predictions and a combination of ice-core gas records: the WD CO_2 (65,000–10,000 years BP); Taylor Glacier $\delta^{13}C$–CO_2 (50,000–35,000 and 22,000–10,000 years BP) (refs. [23,38]); and a reconstruction of mean ocean temperature from ice-core noble gases[45]. The preferred ensemble is selected using those simulations that fall within the top 20% simultaneously for all data constraints ($n = 15$; Fig. 2a). It is important to stress that because the system is fundamentally underconstrained using just the atmospheric gas data, we cannot distinguish the relative contributions of the forcings represented by correlated time series (WD $\delta^{18}O$, Ca and Na) to the overall CO_2 budget. Rather, we are able to illustrate the interactive processes in the Northern and Southern hemispheres that are poorly correlated to each other and how they propagate through the carbon cycle.

Our model is able to explain a large amount of the centennial- and millennial-scale variability observed in the ice-core record. The combined scenario predicts the entire range of variability observed (~45 ppm) from 65,000 to 20,000 years BP (Fig. 2a) as well as our new observation that CO_2 often decreases at the onset of stadials and increases at the onset of interstadials (Fig. 2b). Parsing this into a series of factorial experiments, and then regressing the model predictions against the ice-core data, we find that Southern Hemisphere processes can explain approximately 80% of the observed range in CO_2, and Northern Hemisphere processes can explain the remaining 20%. However, we note that the model does not capture some of the longer-term variability (for example, the data–model discrepancy >60 ka). The Southern Hemisphere processes contribute roughly triangular waveforms that slightly lag the Southern Hemisphere proxies by ~150–250 years using the same lead–lag analysis as previously but using the model forcing and predicted CO_2 as input (Extended Data Figs. 9 and 10). Further differentiation is too uncertain, but we note that the model favours a solution where iron fertilization is a major factor in the glacial–interglacial and millennial-scale CO_2 variability (Extended Data Fig. 6). This is in part due to the timing of the log(Ca), which has the strongest correlation and shortest lag with respect to CO_2 across AIM events (Fig. 1b), and the large increase in log(Ca) and corresponding decrease in CO_2 at 32,000 years BP, which has no corresponding change in $\delta^{18}O$ (Fig. 1a).

Northern Hemisphere and tropical processes contribute small, slow increases in CO_2 (5 ppm) during periods of extended NADW shutdown (Heinrich stadials) and rapid increases in CO_2 during the onset of interstadials (Fig. 2a). The CO_2 increases at interstadials are

driven largely by warming in the region of NADW formation, causing CO_2 outgassing (Extended Data Fig. 8) and a better-ventilated deep Atlantic basin. Crucially, these sources maintain elevated levels of CO_2 and in part counteract a drawdown of CO_2 by Southern Hemisphere sinks. This results in a combined process that appears to lag Antarctic climate by a greater amount than would be expected from a carbon reservoir like the deep Southern Ocean alone. This interplay can be seen in the deep-ocean basin carbon budgets (Fig. 2a). Stadials show the deep Southern Ocean and deep Pacific slowly losing carbon, accompanied by carbon isotope maxima, while the deep Atlantic gains carbon, accompanied by carbon isotope minima (Supplementary Fig. 3). After the onset of interstadial conditions, the deep Pacific gains carbon, the deep Atlantic rapidly loses carbon and warms, and the deep Southern Ocean generally reflects a mixture of these two modes.

The model sometimes produces a shorter apparent lag than the data indicate, suggesting that either the model's response time for the deep ocean is too short or there is a missing CO_2 source in the model during the longer Greenland interstadials (Fig. 2b). Notable examples include DO 14, where the exceptionally long lag is not present in the model, and the 5 ppm CO_2 jump at DO8, where the model does not reproduce the precise timing (Fig. 2a). With the exception of imposed glacial–interglacial changes, we have kept terrestrial fluxes constant, but increased fluxes of terrestrial carbon to the atmosphere have been hypothesized to occur as parts of the Northern Hemisphere rapidly warm during the last deglaciation[46]. Including a terrestrial carbon source to the atmosphere at the onset of interstadials and a sink at the onset of stadials could help to explain the covariation of CH_4 and CO_2. However, atmospheric carbon isotopic constraints suggest the terrestrial biosphere cannot be the sole driver[23,38] of the CO_2 variability but must instead work in conjunction with an oceanic source that is in part driven by temperature. High-resolution radiocarbon and boron isotope data from corals, limited to the last deglaciation, associate the onset of interstadial conditions with rapid ventilation events in both the Atlantic[47] and the Southern Ocean[48]. Both modes of ocean ventilation are plausible sources that our model does not capture in detail due to the coarse resolution but are generally supported by the overall carbon budget (Fig. 2a).

Both the statistical and box-model approaches fail to account for an important feature of the WD CO_2 record—the abrupt centennial-scale increases in CO_2 during several of the Heinrich stadials of the past 70,000 years. They thus appear unrelated to either Antarctic or Greenland climate in a strongly linear way but do correspond to ~50 ppb steps in CH_4 that have previously been linked to Heinrich events and possible Southern Hemisphere methane sources[5] (Fig. 3). Isotopic evidence from CO_2 in Taylor Glacier ice for HS4 and HS1 suggests a ^{13}C-depleted input consistent with a terrestrial source[23,38] or alternatively a rapid flushing of the intermediate ocean driven by enhanced wind stress in the Southern Ocean[49]. There are no obvious rapid increases in CO_2 at Heinrich stadials 6, 5a or 3, which is consistent with the WD CH_4 record and suggests a common mechanism for the abrupt changes that is possibly linked to Laurentide Ice Sheet-specific Heinrich events[5].

Conclusions

Our data show there are at least three major modes of pervasive variability that in aggregate account for CO_2 variability during the last glacial period: (1) the well-known millennial-scale oscillations most likely driven by Southern Ocean processes (2) a centennial-scale source at the onset of DO events that reacts quickly to Northern Hemisphere and tropical climate change, and (3) an additional centennial-scale release of CO_2 during some Heinrich stadials. Our box-model results provide an illustration of how the lead–lag relationship between climate and CO_2 should now be examined with more-realistic, dynamical models, particularly Earth system models capable of simulating the carbon cycle and atmospheric chemistry. Critically, models that aim to provide mechanistic insight into natural carbon cycle feedbacks should consider potential oceanic sources of CO_2 during interstadial conditions and the sensitivity of the terrestrial biosphere to abrupt climate change.

Online content

Any methods, additional references, Nature Research reporting summaries, source data, extended data, supplementary information, acknowledgements, peer review information; details of author contributions and competing interests; and statements of data and code availability are available at https://doi.org/10.1038/s41561-020-00680-2.

Received: 26 March 2020; Accepted: 8 December 2020;
Published online: 4 February 2021

References

1. Dansgaard, W. et al. Evidence for general instability of past climate from a 250-kyr ice-core record. *Nature* **364**, 218–220 (1993).
2. Severinghaus, J. P. Timing of abrupt climate change at the end of the Younger Dryas interval from thermally fractionated gases in polar ice. *Nature* **391**, 141–146 (1998).
3. Huber, C. et al. Isotope calibrated Greenland temperature record over Marine Isotope Stage 3 and its relation to CH_4. *Earth Planet. Sci. Lett.* **243**, 504–509 (2006).
4. Blunier, T. & Brook, E. J. Timing of millennial-scale climate change in Antarctica and Greenland during the last glacial period. *Science* **291**, 109–112 (2001).
5. Rhodes, R. H. et al. Enhanced tropical methane production in response to iceberg discharge in the North Atlantic. *Science* **348**, 1016–1019 (2015).
6. Stocker, T. S., Wright, D. G. & Broecker, W. S. The influence of high-latitude surface forcing on the global thermohaline circulation. *Paleoceanography* **7**, 529–541 (1992).
7. Crowley, T. J. North Atlantic deep water cools the Southern Hemisphere. *Paleoceanography* **7**, 489–497 (1992).
8. Broecker, W. S. Paleocean circulation during the last deglaciation: a bipolar seesaw? *Paleoceanography* **13**, 119–121 (1998).
9. Stocker, T. F. The seesaw effect. *Science* **282**, 61–62 (1998).
10. Barbante, C. et al. One-to-one coupling of glacial climate variability in Greenland and Antarctica. *Nature* **444**, 195–198 (2006).
11. WAIS Divide Project Members. Precise interpolar phasing of abrupt climate change during the last ice age. *Nature* **520**, 661–665 (2015).
12. Indermühle, A., Monnin, E., Stauffer, B., Stocker, T. F. & Wahlen, M. Atmospheric CO_2 concentration from 60 to 20 kyr BP from the Taylor Dome ice core, Antarctica. *Geophys. Res. Lett.* **27**, 735–738 (2000).
13. Noone, D. & Simmonds, I. Sea ice control of water isotope transport to Antarctica and implications for ice core interpretation. *J. Geophys. Res.* **109**, D07105 (2004).
14. Fischer, H. et al. The role of Southern Ocean processes in orbital and millennial CO_2 variations—a synthesis. *Quat. Sci. Rev.* **29**, 193–205 (2010).
15. Wolff, E. W., Rankin, A. M. & Röthlisberger, R. An ice core indicator of Antarctic sea ice production? *Geophys. Res. Lett.* **30**, 2158 (2003).
16. Abram, N. J., Wolff, E. W. & Curran, M. A. J. A review of sea ice proxy information from polar ice cores. *Quat. Sci. Rev.* **79**, 168–183 (2013).
17. Stephens, B. B. & Keeling, R. F. The influence of Antarctic sea ice on glacial–interglacial CO_2 variations. *Nature* **404**, 171–174 (2001).
18. Baumgartner, M. et al. High-resolution interpolar difference of atmospheric methane around the Last Glacial Maximum. *Biogeosciences* **9**, 3961–3977 (2012).
19. Ahn, J. & Brook, E. J. Atmospheric CO_2 and climate on millennial time scales during the Last Glacial Period. *Science* **322**, 83–85 (2008).
20. Bereiter, B. et al. Mode change of millennial CO_2 variability during the last glacial cycle associated with a bipolar marine carbon seesaw. *Proc. Natl Acad. Sci. USA* **109**, 9755–9760 (2012).
21. Anderson, R. F. et al. Wind-driven upwelling in the Southern Ocean and the deglacial rise in atmospheric CO_2. *Science* **323**, 1443–1448 (2009).
22. Skinner, L. C., Fallon, S., Waelbroeck, C., Michel, E. & Barker, S. Ventilation of the deep Southern Ocean and deglacial CO_2 rise. *Science* **328**, 1147–1151 (2010).
23. Bauska, T. K. et al. Controls on millennial-scale atmospheric CO_2 variability during the last glacial period. *Geophys. Res. Lett.* **45**, 7731–7740 (2018).
24. Ahn, J. & Brook, E. J. Siple Dome ice reveals two modes of millennial CO_2 change during the last ice age. *Nat. Commun.* **5**, 3723 (2014).
25. Marcott, S. A. et al. Centennial-scale changes in the global carbon cycle during the last deglaciation. *Nature* **514**, 616–619 (2014).

26. Ahn, J., Brook, E. J., Schmittner, A. & Kreutz, K. Abrupt change in atmospheric CO_2 during the last ice age. *Geophys. Res. Lett.* **39**, L18711 (2012).
27. Gottschalk, J. et al. Mechanisms of millennial-scale atmospheric CO_2 change in numerical model simulations. *Quat. Sci. Rev.* **220**, 30–74 (2019).
28. Marchal, O. et al. Modelling the concentration of atmospheric CO_2 during the Younger Dryas climate event. *Clim. Dyn.* **15**, 341–354 (1999).
29. Köhler, P., Joos, F., Gerber, S. & Knutti, R. Simulated changes in vegetation distribution, land carbon storage, and atmospheric CO_2 in response to a collapse of the North Atlantic thermohaline circulation. *Clim. Dyn.* **25**, 689–708 (2005).
30. Menviel, L., Spence, P. & England, M. H. Contribution of enhanced Antarctic Bottom Water formation to Antarctic warm events and millennial-scale atmospheric CO_2 increase. *Earth Planet. Sci. Lett.* **413**, 37–50 (2015).
31. Ahn, J., Brook, E. J. & Howell, K. A high-precision method for measurement of paleoatmospheric CO_2 in small polar ice samples. *J. Glaciol.* **55**, 499–506 (2009).
32. Sigl, M. et al. The WAIS Divide deep ice core WD2014 chronology—Part 2: annual-layer counting (0–31 ka BP). *Clim. Past* **12**, 769–786 (2016).
33. Buizert, C. et al. The WAIS Divide deep ice core WD2014 chronology—Part 1: methane synchronization (68–31 ka BP) and the gas age–ice age difference. *Clim. Past* **11**, 153–173 (2015).
34. North Greenland Ice Core Project members. High-resolution record of Northern Hemisphere climate extending into the last interglacial period. *Nature* **431**, 147–151 (2004).
35. McConnell, J. R. et al. Synchronous volcanic eruptions and abrupt climate change ~17.7 ka plausibly linked by stratospheric ozone depletion. *Proc. Natl. Acad. Sci. USA* https://doi.org/10.1073/pnas.1705595114 (2017).
36. Markle, B. R., Steig, E. J., Roe, G. H., Winckler, G. & McConnell, J. R. Concomitant variability in high-latitude aerosols, water isotopes and the hydrologic cycle. *Nat. Geosci.* **11**, 853–859 (2018).
37. Bender, M. et al. Climate correlations between Greenland and Antarctica during the past 100,000 years. *Nature* **372**, 663–666 (1994).
38. Bauska, T. K. et al. Carbon isotopes characterize rapid changes in atmospheric carbon dioxide during the last deglaciation. *Proc. Natl Acad. Sci. USA* **113**, 3465–3470 (2016).
39. Marcott, S. A., Shakun, J. D., Clark, P. U. & Mix, A. C. A reconstruction of regional and global temperature for the past 11,300 years. *Science* **339**, 1198–1201 (2013).
40. Shakun, J. D. et al. Global warming preceded by increasing carbon dioxide concentrations during the last deglaciation. *Nature* **484**, 49–54 (2012).
41. WAIS Divide Project Members. Onset of deglacial warming in West Antarctica driven by local orbital forcing. *Nature* **500**, 440–444 (2013).
42. Henry, L. G. et al. North Atlantic ocean circulation and abrupt climate change during the last glaciation. *Science* **353**, 470–474 (2016).
43. McManus, J. F., Francois, R., Gherardi, J. M., Keigwin, L. D. & Brown-Leger, S. Collapse and rapid resumption of Atlantic meridional circulation linked to deglacial climate changes. *Nature* **428**, 834–837 (2004).
44. Elsig, J. et al. Stable isotope constraints on Holocene carbon cycle changes from an Antarctic ice core. *Nature* **461**, 507–510 (2009).
45. Bereiter, B., Shackleton, S., Baggenstos, D., Kawamura, K. & Severinghaus, J. Mean global ocean temperatures during the last glacial transition. *Nature* **553**, 39–44 (2018).
46. Winterfeld, M. et al. Deglacial mobilization of pre-aged terrestrial carbon from degrading permafrost. *Nat. Commun.* **9**, 3666 (2018).
47. Chen, T. et al. Synchronous centennial abrupt events in the ocean and atmosphere during the last deglaciation. *Science* **349**, 1537 (2015).
48. Rae, J. W. B. et al. CO_2 storage and release in the deep Southern Ocean on millennial to centennial timescales. *Nature* **562**, 569–573 (2018).
49. Menviel, L. et al. Southern Hemisphere westerlies as a driver of the early deglacial atmospheric CO_2 rise. *Nat. Commun.* **9**, 2503 (2018).

Methods

Ice-core gas measurements and comparison with previous data. The CO_2 concentrations presented here are quantified using dry standard air calibrated at the National Oceanic and Atmospheric Administration (NOAA) Earth System Research Laboratory (WMOX2007). Nitrogen isotope data ($\delta^{15}N–N_2$) are used to correct the CO_2 data by 1.0–1.4 ppm for gravitational fractionation[33,50]. As atmospheric CO_2 is well mixed over Antarctica, it is expected that offsets between Antarctic ice-core records must arise from preservation effects or methodological differences. On the basis of inter-laboratory comparisons between Law Dome and WD[51] and unpublished inter-calibrations between Oregon State University and the University of Bern laboratories on the same ice from WD, any offset is unlikely to be the result of laboratory methods.

Previously, it was concluded that the WD CO_2 record was elevated by 4 ppm relative to European Project for Ice Coring in Antarctica (EPICA) Dome C during the last deglaciation[25]. With the additional data from the last glacial period, we undertook a comprehensive analysis of the differences between WD and other published records (Extended Data Fig. 1). No single record spans the entirety of the WD record, in large part because the time interval includes the bubble–clathrate transition in most ice cores. This precludes firm conclusions about the exact nature of any offset and whether they vary with time. Broadly, WD is almost always elevated compared with other published records. With the exception of the deglacial data from Taylor Glacier[38], the offset varies from ~2 to 8 ppm (Extended Data Fig. 2). No clear pattern emerges given the numerous variables that might impact the preserved CO_2 given site characteristics (temperature, accumulation, elevation, years since drilling). It is interesting that records from ice above the bubble–clathrate transition (EPICA Dome C (EDC), Taylor Glacier, Taylor Dome, Siple Dome) tend to have lower CO_2 values than other cores that are clathrate ice in Marine Isotope Stage 3 (MIS3) (WD, EDML, Talos Dome, Byrd). Siple Dome, in particular, appears to preserve exceptionally low CO_2 and seems to be in good agreement with high-elevation, cold, low-accumulation sites from EDC and Taylor Glacier. This is somewhat surprising given Siple Dome is one of the warmest and lowest-elevation sites in Antarctica. However, the varying offsets between WD and various Taylor Glacier datasets would suggest that the formation of clathrates is not the only factor and highlights the need to understand whether differences vary with depth/age in the ice. Future research in this vein should focus on the relationship between impurity content, particularly organic carbon, and CO_2 offsets, the role of temperature and accumulation on preservation of the atmospheric signal, and whether offsets emerge in the ice cores relative to the bubble–clathrate transition zone.

Overview of box-model simulations. Our aim with box-model experiments is to arrive at an ensemble of semi-realistic scenarios explaining the carbon cycle history of the last 65,000 years, primarily to examine the implications of various mechanisms for the timing of events we observe in the record. To do this, we use a 14-box ocean/atmosphere/terrestrial biosphere model[38]. Briefly, our scheme is to run the model in a Monte Carlo framework such that a series of forcings are prescribed with variable strengths. From this large suite of simulations ($n=500$), a selection is made by reducing the error between the predictions and key ice-core gas data (Extended Data Fig. 6). We use a total of eight major forcings, two well-constrained changes and three ice-core constraints. The ice-core constraints are atmospheric CO_2 (this study), atmospheric $\delta^{13}C–CO_2$ (refs. [23,38]) and the noble gas-based reconstructions of mean ocean temperature[45]. As such, the system is very underdetermined, so we stress that we derive a plausible, but not definitive, scenario for the last glacial period.

The eight major forcings can be divided into groups related to high-latitude Northern Hemisphere, high-latitude Southern Hemisphere and low-latitude processes. In the high-latitude Northern Hemisphere, we alter North Atlantic/North Pacific SST (by the same magnitude) and NADW formation rate. In the tropics, only low-latitude SST forces the model. In the high-latitude Southern Hemisphere, we force sub-Antarctic SST, Antarctic SST, AABW formation, sub-Antarctic/Antarctic surface levels of resorting PO_4 and Antarctic sea-ice coverage. We also incorporate previous estimates for build-up of reefs and regrowth of the terrestrial biosphere that remain fixed in every experiment. These two factors play a role in the evolution of CO_2 and $\delta^{13}C–CO_2$ during the later part of the last deglaciation and thus do not affect our results, which use data only up to 10,000 years BP. However, they play a major role during the Holocene[44] and are key to the overall data–model agreement (albeit not formally analysed here in the RMSE reduction) (Extended Data Fig. 6). We apply carbon cycle processes only in the models that have been well characterized for their atmospheric CO_2 and carbon isotope responses and could be confirmed as realistic with other box models or isotope-enabled dynamical models. We thus did not consider changes in North Atlantic sea ice as a possible driver in our ensemble but have analysed it in a separate set of experiments (see Supplementary Information).

We use a series of well-resolved proxy records, mostly from ice cores, to form the basis of our carbon cycle-forcing time series. Each forcing time series preserves the underlying structure of the data but is input into the model at each simulation with a random scaling between 50% and 100% of the maximum effect allowed by the box model (Extended Data Fig. 6, left panel), except for temperature records used as SST forcings, which are varied randomly between ±20% of their reported absolute G–IG range (Extended Data Fig. 6, middle panel). The maximum scaling parameters and their respective impacts on atmospheric CO_2 are shown in Extended Data Fig. 8 and reported in Extended Data Fig. 7. For example, the rate of AABW formation in a given model run will track the record of WD $\delta^{18}O$ whereby some runs result in a near-complete shutdown in the Last Glacial Maximum, some runs only reach 50% of the Last Glacial Maximum level and most fall somewhere in this range.

High-latitude Northern Hemisphere forcings. In the Northern Hemisphere, the strength of NADW in the model is derived from the Bermuda rise Pa/Th record (Extended Data Fig. 6, left panel). We made a few minor adjustments to the Bermuda rise age model (<±500 years) to align the resumption in NADW to the onset of interstadial events in Greenland. The maximum NADW input varies by about 10 Sv in a series of millennial-scale events that are most pronounced during the 'Heinrich stadials'. The SST of the two northern high-latitude oceans boxes (North Atlantic and North Pacific) are driven by the temperature stacks[39,40] from 22 ka to present and the NGRIP $\delta^{18}O$ scaled to deglacial change before 22 ka. As with all SST forcings in our model, the temperature of the polar ocean is restricted to a minimum of near-freezing conditions (−2 °C). This scaling results in temperature swings up to 2 °C during MIS3, a range permitted but not particularly well constrained by joint model–proxy inversion for the North Atlantic. The NGRIP record used is an age model consistent with the WD record as proposed in ref. [11].

Low-latitude (tropical) forcings. The tropical changes are driven solely by SST changes in the low-latitude Atlantic and Pacific boxes (Extended Data Fig. 6, middle panel). Temperature is forced using the deglacial SST stacks but then extended into MIS3 using the total radiative forcing from the WD greenhouse gas data. This results in millennial-scale variability of about 1 °C during MIS3. This is perhaps the most difficult assumption to check because, to our knowledge, there are no records of tropical SST that can be conclusively tied to the ice-core records on the submillennial timescale throughout MIS3. However, because the temperature of the deep ocean is largely set in the polar regions, the changes in the tropical SST affect mostly the simulated changes in $\delta^{13}C–CO_2$ via changes in carbon isotope fractionation during air–sea gas exchange.

High-latitude Southern Hemisphere forcings. The Southern Hemisphere changes are largely derived from WD proxies. This is a major advantage of our study in that we are able to directly compare the ice-phase proxies of carbon cycle processes with the gas-phase record of atmospheric CO_2, including passing these proxies through our model. Our aim is to derive reasonable histories for the four major players in the Southern Ocean carbon cycle: temperature, ocean circulation/stratification, nutrient utilization and air–sea gas exchange (including sea-ice coverage).

Quantitative proxies for Southern Ocean circulation in the past are limited. Most evidence comes from indirect proxies that are convolved with other factors. For example, opal productivity has been tied to upwelling around Antarctica but is also influenced by nutrient utilization. Benthic ^{14}C is a useful indicator of the overturning rate of the deep ocean but is also controlled by air–sea gas exchange. Benthic ^{13}C reflects both the input of respired carbon to the deep ocean and the mixing of different water masses. Rather than use any one proxy as a direct, linear forcing, we use our model to simulate these indirect proxies and therefore can use them as post hoc constraints (see Supplementary Information for an in-depth analysis). WD $\delta^{18}O$ is used as the initial input for the overturning rate of AABW formation because it is sensitive to a combination of West Antarctic temperature and sea-ice extent and thus partially reflects the heat and salt budget of the Southern Ocean. The log of WD Ca, a proxy for mineral-dust transport to Antarctica that plausibly contributes to iron fertilization in the Southern Ocean, is used to scale nutrient utilization (restoring PO_4 levels) in the sub-Antarctic and Antarctic surface ocean basins. The log of WD Na, a promising proxy for sea ice, is used to scale sea-ice extent over the Antarctic surface ocean and also affects the efficiency of the biological pump in this region, with greater sea-ice coverage lowering the total export productivity.

Ca and Na are proxies for dust delivery and sea-ice extent, respectively, that have been ground-truthed with marine records[52–54] or supported by models[55]. However, it is also thought that these ice-core proxies in the Antarctic, including the WD record[36], can be influenced by hydrological processes during transport and are thus not driven solely by sources changes. In the case of Ca, we make no implicit assumptions as to changes in source and assume only that variability in Antarctica is linearly related to the dust delivery in the Southern Ocean as supported by the marine Fe flux. In the case of Na, we assume a linear relationship with sea-ice area and thus would require near-field changes in the sea-ice source of Na. Our choice to use $\delta^{18}O$ as a forcing for the AABW formation rate, which in part drives upwelling in the Antarctic Ocean, is more difficult to ground-truth as there are limited direct proxies for overturning. Here we are informed by dynamical models that demonstrate a tight coupling among Antarctic temperature, atmospheric CO_2 and AABW formation when a buoyancy forcing is applied to the Southern Ocean[30].

Selecting the model ensemble and factorial experiments. We run 500 simulations of the model with random variations in all the scaling parameters. For each experiment, we calculate the RMSE between the model prediction and ice-core data. For constraints, we use the WD CO_2 record from 65 to 10 ka; the

Taylor Glacier $\delta^{13}C$–CO_2 record in two intervals, from 50 to 35 ka and from 25 to 10 ka; and the WD mean ocean temperature reconstruction from 25 to 10 ka (Extended Data Fig. 6, right panel). Both the model predictions and ice-core data are normalized by their means before the RMSE calculation. We then select all the experiments that fall within top 20% for all three constraints. This selection, referred to as the 'combined scenario', is plotted in Extended Data Fig. 6 with the initial range of inputs, the range of inputs after selection of the combined scenario, and the model predictions with data constraints.

We then break the full scenario into high-latitude Northern Hemisphere/low-latitude and Southern Hemisphere components by running factorial experiments using the suite of scaling parameters determined in the combined scenario. The Northern Hemisphere/low-latitude ensemble is forced with North Atlantic, North Pacific and low-latitude SST along with NADW formation. The Southern Hemisphere ensemble is forced with sub-Antarctic and Antarctic SST along with AABW formation, nutrient utilization and Antarctic sea ice.

Lead–lag and stacking analysis. The analysis of the lead–lag between CO_2 and the various ice-core proxies is done with a simple correlation analysis. A Monte Carlo method is used to account for analytical errors and uncertainty in the delta age. All time series are first smoothed with a series of splines that include error in the gas data. The splines are generated using Matlab cubic spline function csaps, with smoothing parameters between 1e-5 and 1e-6. On the basis of the average resolution of the input datasets, these correspond to spline cut-off periods between about 250 and 450 years. The ice-phase data are similarly smoothed but also varied by the uncertainty in the delta-age history[33] ($n=1{,}000$). All data are then linearly detrended over the selected correlation window (65 to 25 ka). The lead–lag correlation is calculated by shifting the proxy time series between −2,000 years and +2,000 years at 20-year time steps for the entire ensemble of possible gas- and ice-phase histories. The resulting errors on the linear regression values for R^2 at each lag are reported as the 5th to 95th percentile range of all solutions. Similarly, the lag at which the R^2 reaches a maximum is shown as the 5th to 95th percentile range graphically in Fig. 1b and in Extended Data Fig. 3. The same analysis is applied to the box-model forcing and predictions, including the various factorial experiments shown in Extended Data Fig. 8. The results are reported in Extended Data Fig. 9 and visualized in Extended Data Fig. 10. The CO_2 residual is calculated in a similar Monte Carlo framework (detrended data, analytical errors) but uses only the lag that the linear regression produces the maximum R^2 between the WDC $\delta^{18}O$ and CO_2 (lag = 580 years).

We also analysed lead–lag relationships by passing each proxy time series through a one-box model with variable e-folding timescales (0–2,000 years at 10-year increments). The resulting time series are then compared with the CO_2 data to find the e-folding timescales that maximize correlation (Extended Data Fig. 4). This type of signal processing and visualization is similar to that employed in an analysis of the bipolar seesaw[56] and to disentangle the impact of regional climate variability on atmospheric CO_2 (ref. [57]). The same Monte Carlo-based approach is employed to include uncertainties in the data and chronologies. The results are in broad agreement with the simple correlation plots, which gives us confidence that both analyses yield the characteristic timescales of the carbon cycle response.

We constructed the mean evolution of the CH_4, CO_2 and $\delta^{18}O$ data after the onset of both a stadial and interstadial (Figs. 1c and 2c) by stacking the spline-smoothed curves into 10-year bins. Time zero is set to either the rise or fall in CH_4, and all the signals are reported as anomalies from the mean value during the preceding interval (250 years for stadials, 500 years for interstadials). The reported range is the 1σ standard error between all the different events for each bin. These ranges thus constrain the mean response of the system and do not reflect variability between each event.

We also derived the maximum CO_2 response at each individual DO interstadial for statistical analysis (Extended Data Fig. 5) using the same smoothing procedure. Here the maximum CO_2 and CH_4 responses at an interstadial are the difference between the maximum value reached during the interstadial window and the mean values during the stadial period immediately preceding the transition (500 years). To determine whether the presence of a Heinrich event in the preceding stadial had any apparent influence on the CO_2 response, we used a t test with groups of Heinrich stadials ($n=6$) and non-Heinrich stadials ($n=9$) (Extended Data Fig. 5). The test showed no significant difference ($P=0.075$). Analysis of the statistical links between CO_2 and the length of previous stadial, length of interstadial and maximum CH_4 utilized correlation analysis (Extended Data Fig. 5) with only the correlation between CO_2 and length of interstadial showing any significant correlation ($r=0.54$, $P=0.04$).

Data Availability

The WAIS Divide CO_2 data are publicly available at the NOAA NCEI Database (https://www.ncdc.noaa.gov/paleo/study/31772) and US Antarctic Program Data Center (https://www.usap-dc.org/view/dataset/601337).

Code Availability

Model results are summarized in the supplemental material, and the entire suite of Monte Carlo simulations and box-model code is available from T.K.B. upon request.

References

50. Severinghaus, J. P. Low-res $\delta^{15}N$ and $\delta^{18}O$ of O_2 in the WAIS Divide 06A Deep Core (USAP, 2015); https://doi.org/10.7265/N5S46PWD
51. Ahn, J. et al. Atmospheric CO_2 over the last 1000 years: a high-resolution record from the West Antarctic Ice Sheet (WAIS) Divide ice core. *Glob. Biogeochem. Cycles* **26**, GB2027 (2012).
52. Anderson, R. F. et al. Biological response to millennial variability of dust and nutrient supply in the Subantarctic South Atlantic Ocean. *Philos. Trans. A* **372**, 20130054 (2014).
53. Lamy, F. et al. Increased dust deposition in the Pacific Southern Ocean during glacial periods. *Science* **343**, 403–407 (2014).
54. Jaccard, S. L., Galbraith, E. D., Martínez-García, A. & Anderson, R. F. Covariation of deep Southern Ocean oxygenation and atmospheric CO_2 through the last ice age. *Nature* **530**, 207–210 (2016).
55. Levine, J. G., Yang, X., Jones, A. E. & Wolff, E. W. Sea salt as an ice core proxy for past sea ice extent: a process-based model study. *J. Geophys. Res. Atmos.* **119**, 5737–5756 (2014).
56. Stocker, T. F. & Johnsen, S. J. A minimum thermodynamic model for the bipolar seesaw. *Paleoceanography* **18**, 4 (2003).
57. Bauska, T. K. et al. Links between atmospheric carbon dioxide, the land carbon reservoir and climate over the past millennium. *Nat. Geosci.* **8**, 383–387 (2015).
58. Monnin, E. et al. Atmospheric CO_2 concentrations over the last glacial termination. *Science* **291**, 112–114 (2001).
59. Schmitt, J. et al. Carbon isotope constraints on the deglacial CO_2 rise from ice cores. *Science* **336**, 711–714 (2012).
60. Eggleston, S., Schmitt, J., Bereiter, B., Schneider, R. & Fischer, H. Evolution of the stable carbon isotope composition of atmospheric CO_2 over the last glacial cycle. *Paleoceanography* **31**, 434–452 (2016).
61. Neff, P. D. A review of the brittle ice zone in polar ice cores. *Ann. Glaciol.* **55**, 72–82 (2014).

Acknowledgements

This work was funded by NSF grant 0944764 to E.J.B. and Royal Society University Research Fellowship (grant URF\R1\180366) to T.K.B. We thank M. Kalk and T. Alig for assistance in measuring the CO_2 data. We appreciate the support of the WAIS Divide Science Coordination Office at the Desert Research Institute (DRI) of Reno, Nevada, and the University of New Hampshire for the collection and distribution of the WAIS Divide ice core and related tasks (NSF grants 0230396, 0440817, 0944348 and 0944266). Additional support for this research came from the NSF Office of Polar Programs through their support of the Ice Drilling Program Office and the Ice Drilling Design and Operations group; the US National Ice Core Laboratory, for curation of the core; and the 109th New York Air National Guard, for airlift to Antarctica.

Author contributions

T.K.B. and S.A.M. contributed equally. E.J.B. and S.A.M. designed the study. S.A.M. measured the CO_2 data and performed the preliminary analysis. T.K.B. performed time series and modelling analyses and led the writing of the paper with input from S.A.M. and E.J.B.

Competing interests

The authors declare no competing interests.

Additional information

Extended data is available for this paper at https://doi.org/10.1038/s41561-020-00680-2.

Supplementary Information The online version contains supplementary material available at https://doi.org/10.1038/s41561-020-00680-2.

Correspondence and requests for materials should be addressed to T.K.B. or S.A.M.

Peer review information *Nature Geoscience* thanks Julia Gottschalk and the other, anonymous, reviewer(s) for their contribution to the peer review of this work. Primary Handling Editor: James Super.

Reprints and permissions information is available at www.nature.com/reprints.

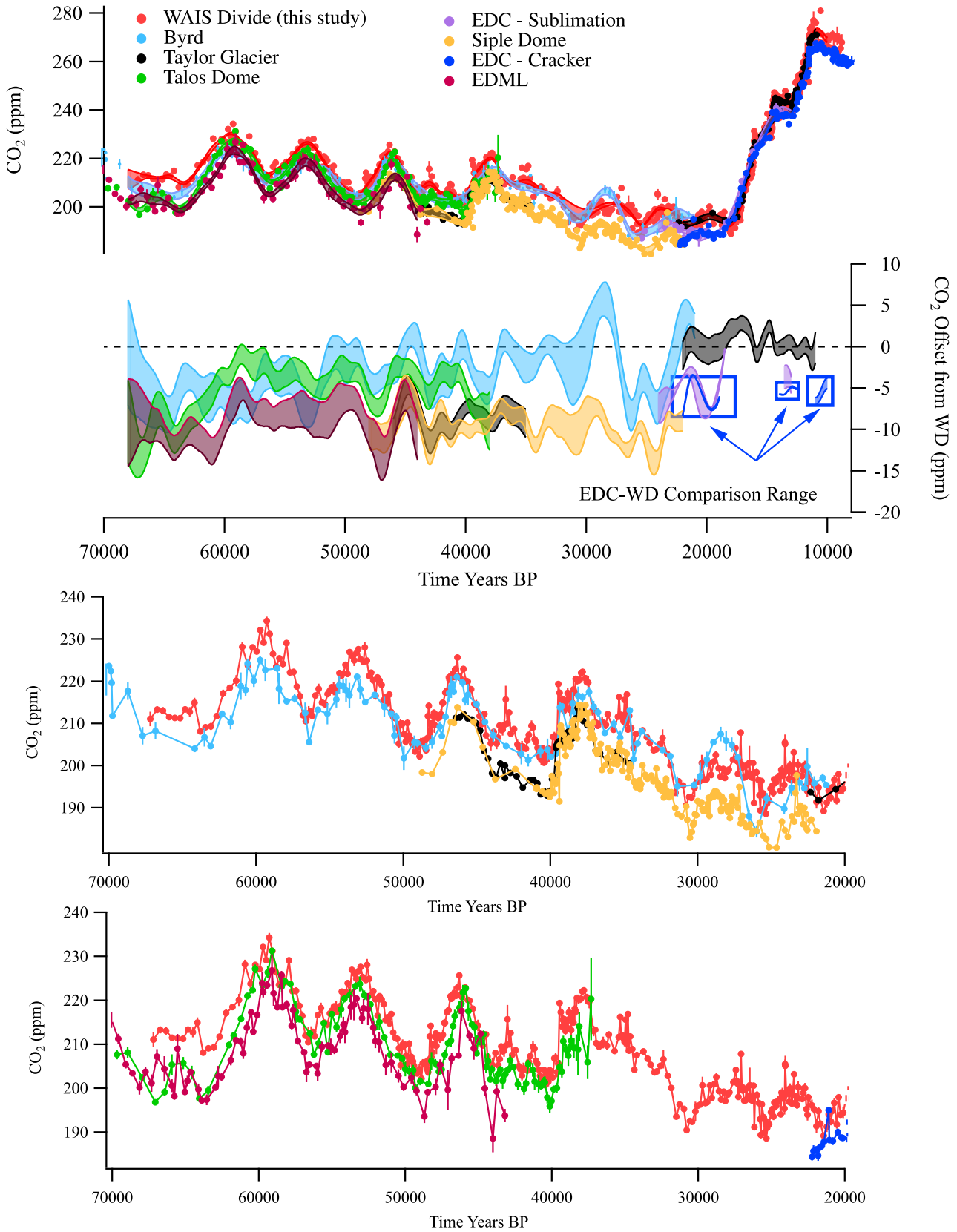

Extended Data Fig. 1 | A comparison of the WD to other ice core records of atmospheric CO_2. A comparison of ice core CO_2 records including WD (this study), Byrd[19], Taylor Glacier[23,38], Talos Dome[20], EDC (mechanical crushing[58] and sublimation data[59]), Siple Dome[24,26] and EDML[20]. All the ice core records have been smoothed with splines to preserve the millennial-scale variability and then subtracted from the WD record to show any offsets. Note that millennial-scale differences in the CO_2 offset are susceptible to small errors in the various ice core chronologies (AICC2012) relative to the WD2014. Sub-panels show the raw data for each individual core record.

Core	Reference	Method	Overall Time Interval	Overlap Interval (ka)	Site Characteristics			Bubble or Clathrate?	Year Drilled	CO_2 offset (ppm)
					Temp. (°C)	Acc. (m ice a-1)	Elevation (m)			
WAIS Divide	This study	OSU Cracker	-	-	–30	0.22	1766	Clathrate	2006–11	0
Taylor Glacier	Bauska et al., 2016	OSU Ice Grater	Deglacial*	11-22	Similar to Taylor Dome			Bubble	2010-2011	0.5
EDC	Monnin et al., 2001	Bern Cracker		10-22	–54	0.036	3233	Bubble	1999–2004	-5.6
EDC	Schmitt et al., 2012	Sublimation		13-25						-5
Siple Dome	Ahn et al., 2014	OSU Cracker	MIS3	22-49	–25	0.11	620	Bubble	1997–99	-8.3
Taylor Glacier	Bauska et al., 2018	OSU Ice Grater		35-46	Similar to Taylor Dome			Bubble	2013-2014	-8.3
Talos Dome	Bereiter et al., 2012	Bern Cracker		37-68	–41	0.08	2318	Clathrate	2005–07	-4.1
EDML	Bereiter et al., 2012	Bern Cracker		44-68	-44	0.064	2892	Clathrate	2000–06	-7.8
Taylor Dome**	Indermuehle et al., 2000	Bern Cracker		19-63	-43	0.06	2375	Bubble	1993–94	-4.9
Byrd	Ahn et al., 2008	OSU Cracker		21-68	–28	0.14	1530	Clathrate	1966–67	-1.8

Extended Data Fig. 2 | Mean differences in ice core CO_2 relative to the WD Record. *Note only plateaus in CO_2 used for comparison **Original Taylor Dome[12] timescale is too uncertain to quantify millennial-scale offsets. See Neff, 2014 for details on site data[61].

X	Y	Maximum R^2	Median	5% CI	95% CI
WD CH_4	WD CO_2	0.46	-80	-60	-120
WD Ca		0.69	360	460	300
WD Na		0.48	460	540	380
WD $\delta^{18}O$		0.6	580	650	500
NGRIP $\delta^{18}O$		0.33	40	60	0

Extended Data Fig. 3 | Lead-lag correlation analysis of ice core data with percentile ranges. Median and confidence intervals reported in years.

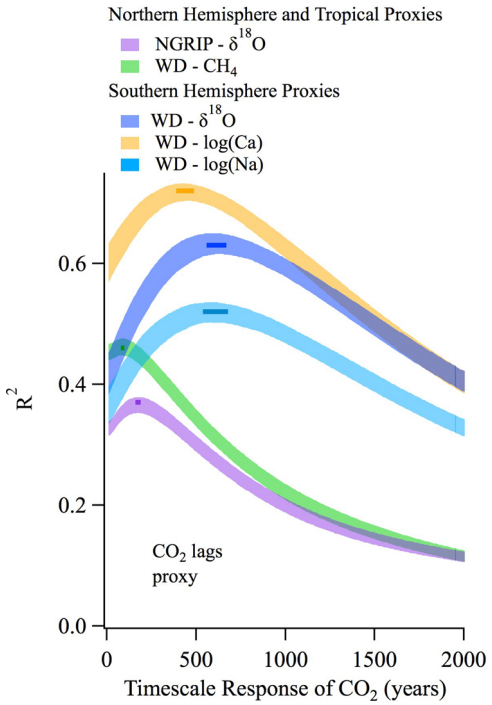

Extended Data Fig. 4 | Alternative lead-lag analysis using one-box models with variable e-folding timescales. The results of correlation of the various ice core proxy time-series against atmospheric CO_2 after being passed through a series of one-box models. The x-axis shows the variable e-folding timescales of each run. Shading shows the uncertainty introduced from Monte Carlo error estimates in the delta-age history (90% CI) as in Fig. 1b (main text). The maximum reached in each curve indicates the apparent lead-lag with the horizontal bars indicate the range in maximum R^2 values from the delta-age histories.

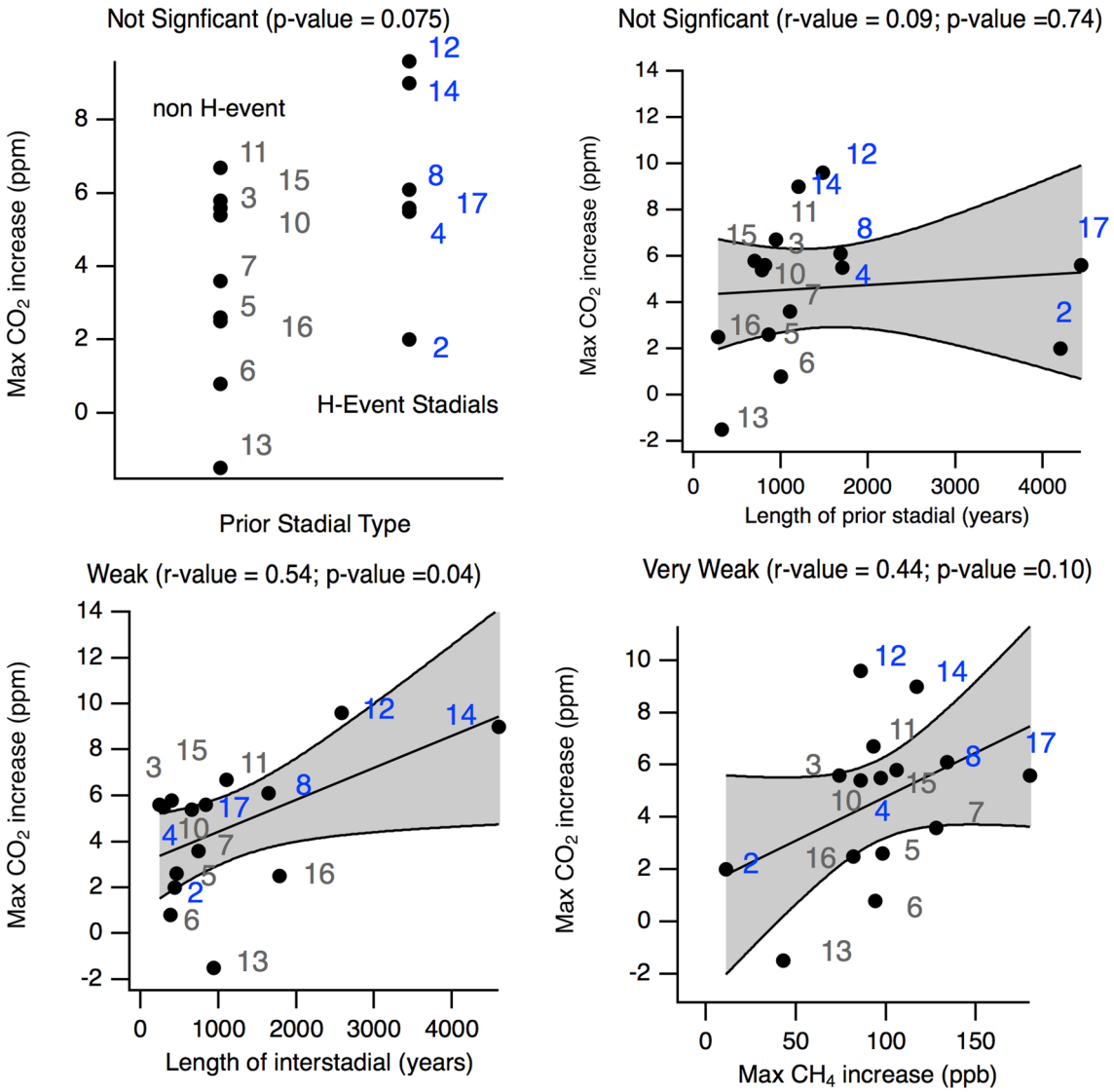

Extended Data Fig. 5 | T-test and correlation analysis of CO_2 response at onset of DO interstadials. Individual interstadials are indicated with black marker and are labeled such that interstadials after an H-event are in blue and all others are labeled in grey. Grey shading shows the 95% confidence interval for the fits of the linear regressions.

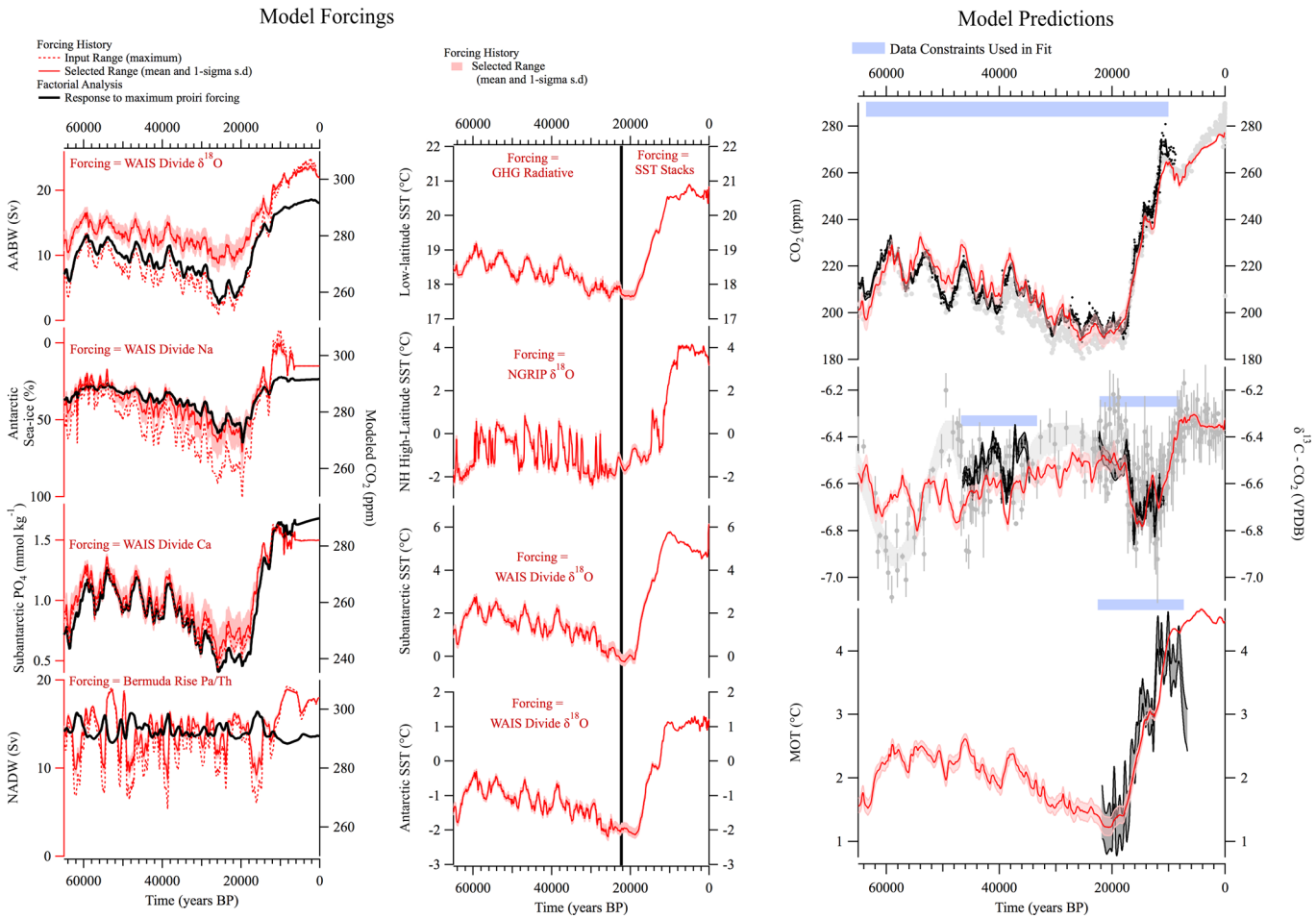

Extended Data Fig. 6 | Objective construction of the model ensemble solution. Left panel. The forcings that enter the model with variable scaling (AABW formation scaled to WD-δ^{18}O Antarctic sea-ice extent scaled to the log of WD Na, Subantarctic PO_4 scaled to WD-Ca, and NADW formation scaled to Bermuda Rise Pa/Th, not shown Antarctic PO_4 scaled to a combination of WD-Ca and sea ice extent). The maximum possible forcing is shown with the dotted red line along with the associated model response of atmospheric CO_2 (black line). The red shading shows the range of forcings (mean and 1-sigma) that produce model predictions consistent with the ice core data (that is the 'combined scenario'). The middle panel shows the same 1-sigma range for temperature forcings in the 'combined scenario'. The right panel shows various model predictions including those that are used to select the 'combined scenario' constraint: atmospheric CO_2, atmospheric $\delta^{13}C$-CO_2 (including spline-smoothed data from refs. [44,59,60]) and mean ocean temperature (MOT). All model results are slightly offset to match interglacial values in the data. Blue bars show the temporal range used in for each data constraint.

		AIM4		G-IG (20-10ka)	
Forcing	Proxy Scaling	Change in Forcing	Change in CO_2	Change in Forcing	Change in CO_2
Max AABW	2.5 Sv/per mil	6 Sv	10 ppm	17 Sv	28 ppm
Max Iron Fertilization	-0.45 PO_4 mmol m^{-3}/ log(Ca) ppb	0.3 mmmol m^{-3}	11 ppm	1.1 mmol m^{-3}	49 ppm
Max Antarctic Sea ice	-60% fraction of sea ice free / log(Na) ppb	25%	5 ppm	100%	23 ppm
Max NADW	-430 Sv / Pa/Th ratio	10 Sv	8 ppm	10 Sv (at HS1)	8 ppm (at HS1)
Mean SST	Variable*	0.6°C (MOT)	8 ppm	2.8°C (MOT)	32 ppm

Extended Data Fig. 7 | Maximum Proxy-to-Forcing Scaling Parameters and Maximum Predicted Changes in CO_2. *SST forcing is applied in the surface boxes but for convenience we report the predicted changes in mean ocean temperature (MOT).

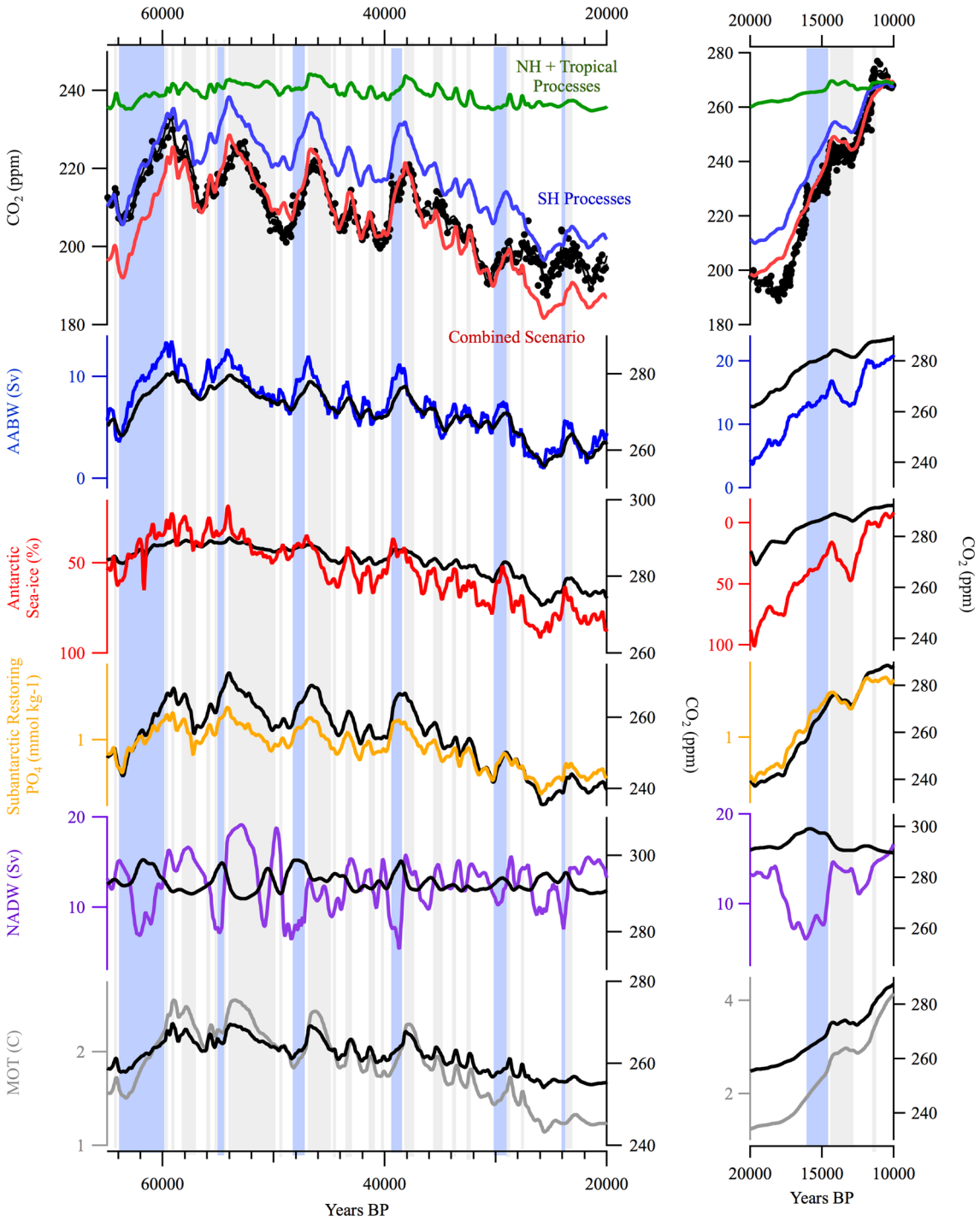

Extended Data Fig. 8 | Maximum effect of the major forcings in the full model ensemble. The upper limit of forcings that enter the model prior to RMSE fitting are plotted on the left axes with the exception of temperature which is shown as the predicted change in MOT for the mean changes in temperature. The colours of the axes correspond to the colour of the trace (AABW = blue; Southern Ocean phosphate = orange; NADW = purple; temperature = grey). The corresponding predicted changes in CO_2 to are plotted against the shown on the right axes in black. The figure is divided between the last glacial period on the left and the deglaciation on the right with larger ranges for all vertical axes during the deglaciation.

X	Y	Maximum R^2	Median Lag (years)
Factorial Experiments			
AABW Formation (WD $\delta^{18}O$)	Respective Factorial CO_2	0.92	260
Subantarctic PO_4 "Iron Fert." (WD Ca)		0.95	140
Antarctic Sea ice (WD Na)		0.82	180
NADW (Pa/Th)		0.92	320
North Atlantic Temperature (NGRIP $\delta^{18}O$)		0.56	40
Combined Scenario			
AABW Formation (WD $\delta^{18}O$)	Combined CO_2	0.78	380
North Atlantic Temperature (NGRIP $\delta^{18}O$)		0.57	-80

Extended Data Fig. 9 | Lead-lag correlation analysis of model forcing and predicted CO_2. Lead-lag correlations for all model factorial experiments in which CO_2 is driven soley by one forcing and lead-lag analysis of the combined scenario with forcings inputs from WD $\delta^{18}O$ and NGRIP $\delta^{18}O$ combined scenario.

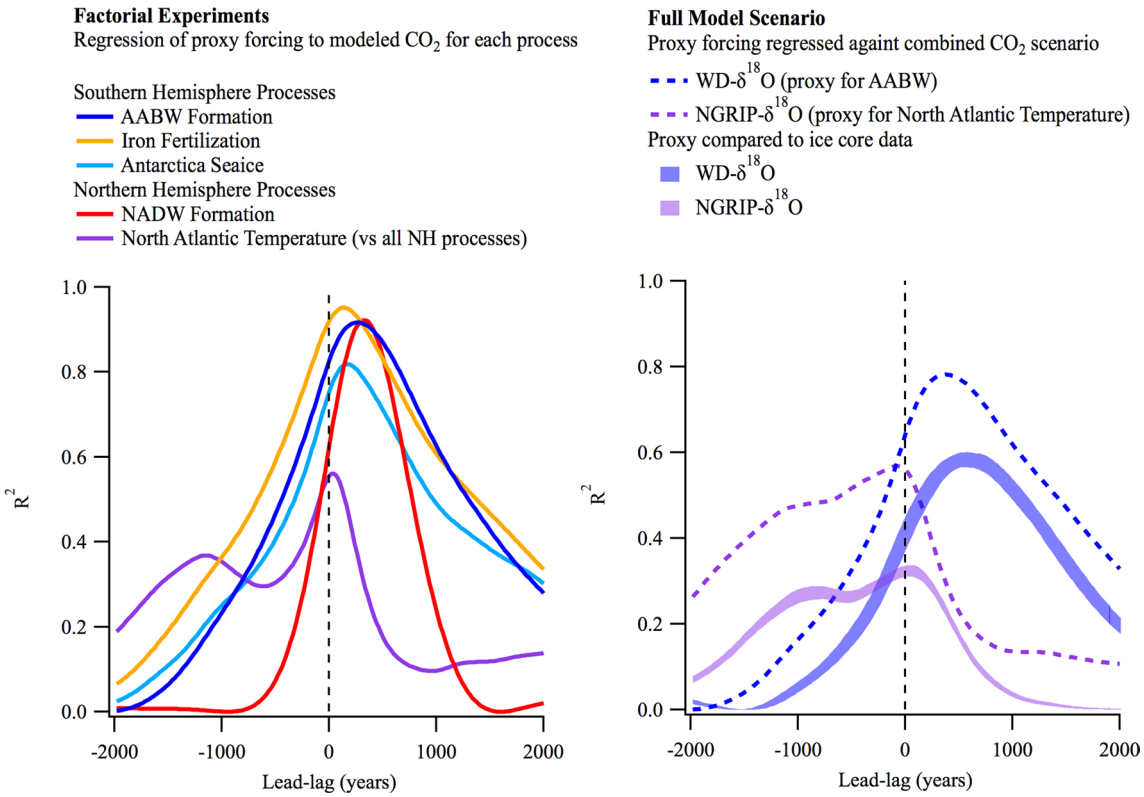

Extended Data Fig. 10 | Lead-lag analysis of model forcing and predictions with comparison to observations. Left panel. Lead-lag correlation of factorial model experiments between proxy forcing and simulated CO_2. Factorial experiments include: AABW formation (dark blue); 'Iron Fertilization'/nutrient utilization (yellow); Antarctic sea ice extent (light blue); NADW formation (red); North Atlantic temperature (purple). Right panel. Lead-lag correlation of the WD-$\delta^{18}O$ (dash dark blue) and NGRIP- $\delta^{18}O$ (dashed purple) that enter the model as forcings against simulated CO_2 in the 'combined scenario'. This mimics the lead-lag correlation performed on the real ice core data and presented in the main body of the text between WD-CO_2 and WD- $\delta^{18}O$ (shaded blue envelope) and WD-$\delta^{18}O$ and NGRIP-$\delta^{18}O$ (shaded purple envelope).